Int J Fract (2010) 162:187–204
DOI 10.1007/s10704-010-9472-y

ORIGINAL PAPER

Shear and tensile plastic behavior of austenitic steel TRIP-120 compared with martensitic steel HSLA-100

F. Latourte · Z. Feinberg · L. F. Mori · G. B. Olson · H. D. Espinosa

Received: 14 August 2009 / Accepted: 2 March 2010 / Published online: 25 March 2010

Abstract The mechanical performance of TRIP-120, a novel transformation induced plasticity steel alloy, is evaluated for different loading cases and strain rates. The performance is compared with HSLA-100, a low-alloy steel developed by the United States Navy and currently used in naval hulls. The response of these materials under uniaxial tension and shear was investigated to the point of fracture at isothermal and adiabatic conditions. TRIP-120 shows a significant improvement in dissipated energy at fracture compared to HSLA-100. SEM images of ductile fracture surfaces for tensile and torsion samples of both TRIP-120 and HSLA-100 are compared, and the presence of transformed martensite in the TRIP-120 dynamic torsion specimens is confirmed with optical microscopy and magnetometry.

Keywords TRIP steels · Martensitic steels · Shear bands · Dynamic fracture · Phase transformation

F. Latourte · L. F. Mori · H. D. Espinosa (✉)
Department of Mechanical Engineering, Northwestern University, 2145 Sheridan Road, Evanston, IL 60201, USA
e-mail: espinosa@northwestern.edu
URL: http://clifton.mech.northwestern.edu/∼espinosa/

Z. Feinberg · G. B. Olson
Department of Material Science, Northwestern University, 2145 Sheridan Road, Evanston, IL 60201, USA

Present address:
L. F. Mori
DIMNP, Università di Pisa, via Diotisalvi 2, 56126 Pisa PI, Italy

Introduction

Numerous applications demand high strength steels with high flow stability and uniform ductility in torsion and shear. Blast and fragment protection in military and civilian applications, e.g., transportation requires maintaining the integrity of structures while simultaneously minimizing their weight. Using the concepts of predictive materials science, materials have been designed to exhibit these desired properties by achieving specific chemical compositions and microstructures. After designing novel alloys, prototype evaluation is required to validate that the desired property objectives have been met. Our objective in this work is to gain insight into the mechanical behavior of new steel alloys for applications involving low weight structures subjected to impulsive loads.

In the investigation of impulsive loads, it is important to monitor and characterize dynamic shear bands (DSB) resulting from damage-induced or thermomechanical instabilities. These appear at high strain rates after an initial uniform plastic deformation. The formation of DSB represents a critical failure mode for many structural metals under dynamic loading conditions as a result of shear localization and should be avoided or delayed to improve the integrity of structures subjected to extreme loadings (Hartley et al. 1987). One example, the "plugging" mode observed in ballistic penetration and important to fragment protection is shown to operate by plastic instability in a local stress state near pure shear (Vernerey et al. 2006). Shear bands nucleate

at a local defect or material inhomogeneity that triggers an enhanced local plastic deformation and subsequent local heating (Duffy and Chi 1992). Once localization occurs in a structure, the heat is produced more rapidly than it can be dissipated by conduction, leading to the adiabatic heating of the structural material and further contributing to a loss in stability (Liao and Duffy 1998). Batra and Kim found that higher thermal conductivity delays the initiation process and subsequently slows down the development of DSB (Batra and Kim 1991). Shear bands usually form in high-strength materials, particularly in materials with low strain rate sensitivity, high thermal softening rate, and low thermal conductivity (Hartley et al. 1987). Rittel and Wang have shown different influences of thermal softening in DSB nucleation for MA50 and Ti6Al4V alloys (Rittel and Wang 2008). Recent work has shown an important role of damage mechanisms such as microvoid softening making localization stress-state dependent (Vernerey et al. 2006).

To avoid the deleterious effects of shear bands, Saha and Olson (2007) developed a high performance martensitic steel BlastAlloy 160 (BA-160) to delay shear instabilities and achieve superior resilience. BA160, with a yield stress of 160 ksi (1,100 MPa), a uniform elongation at failure of 5.7% in quasi-static tension and a Charpy impact toughness of 176 J at room temperature (Saha et al. 2007), was developed based on the assumption that toughness is the critical material property to be improved in order to sustain impulsive loadings. However, recent work has shown that uniform ductility is a concurrent limiting property for blast resistance, provided that the toughness is above the critical threshold to avoid shattering. Previous studies have attempted to design materials combining high strength, high toughness, high uniform ductility, and high shear resistance by exploiting transformation-induced plasticity (TRIP) (Zackay et al. 1967) in austenitic steels (Angel 1954; Olson and Cohen 1986; Patel and Cohen 1953). The transformation of austenite into martensite is influenced by temperature, applied stress, composition of the alloy, strain rate, and loading history. Prior deformation of the austenite phase (Bhandarkar et al. 1972; Stavehaug 1990) can be tailored to stabilize plastic flow and resist necking conditions (Kohn 1976) to increase the ultimate tensile strength σ_u. Shear tests have demonstrated a significant effect of transformation plasticity in retarding shear localization (Haidemenopoulos et al. 1989a). Based on this body of knowledge, a new TRIP steel, TRIP-120, was designed to exhibit superior toughness, higher flow stability and uniform ductility in tension and shear (Sadhukhan 2008).

The behavior of austenitic TRIP steels at high loading rates has not been widely reported. The behavior of multiphase TRIP700 steel has been compared to DP600, a ferrite/bainite dual phase steel by Curtze et al. (2009), over a wide range of strain rates and temperatures, highlighting the superior performance of the TRIP700 in terms of total energy absorption and elongation. A study conducted by Lacroix et al. (2008) compared the fracture toughness of two TRIP steels to that of two dual phase steels. This work describes the TRIP steel fracture toughness in terms of crack tip intervoid ligament work consistent with the flow stabilizing mechanism demonstrated by Socrate (1995) and Olson (1995). Prior research demonstrated the advantages of employing TRIP steels for crash absorption structures and automobile applications; however, limited amount of work has been performed to determine their ultimate failure modes.

The objective of this paper is to characterize the quasi-static and dynamic behavior of a novel TRIP steel (TRIP-120) and to compare it to the conventional martensitic steel HSLA-100 currently used in naval hulls. First, the design of the two steels investigated in this study is described. Second, the experimental methods used to compare the mechanical performance of the two steels are introduced. In the third section, the behavior of the two steels in tension at various loading rates is examined. In the fourth section, the torsion behavior is characterized from both a macroscopic point of view and also on a shorter length scale to investigate shear band formation. High-speed images of the gage surface of the torsion samples are recorded during testing to compute the local strain and monitor the onset of shear band formation. In the last section, post fracture analyses conducted on TRIP-120 and HSLA-100 are discussed. SEM images of fracture surfaces are used to interpret the failure modes of the two steels, and optical microscopy and magnetometry are used to determine the fraction of transformed martensite in the TRIP steel.

1 Steel design

1.1 HSLA-100

The high-strength low-alloy steel HSLA-100 was developed by the United States Navy in the early

Table 1 Chemical composition of TRIP-120 and HSLA-100 in weight percent

	TRIP-120	HSLA-100
Cr	3.986	0.55
Ni	23.542	3.55
Mo	1.245	0.59
Ti	3.029	–
V	0.319	–
Al	0.163	0.03
C	0.01	0.04
Mn	–	0.84
B	0.0125	–
N	10 ppm	128 ppm
Si	–	0.26
Cu	–	1.58
Nb	–	0.029
Fe	Balance	Balance

1990s to reduce fabrication costs in ship construction (Czyryca et al. 1990a,b,c; Nichols 1990; Sawhill 1990). This material has similar strength (a yield stress of 100 ksi or 689 MPa) and toughness to the alloy it replaced—HY-100. HSLA-100 was designed with reduced carbon content in order to make it weldable without preheat, which in turn reduces fabrication costs with respect to HY-100. To compensate the reduced carbon content, copper was added to provide an additional precipitation strengthening mechanism (Das et al. 2006; Dunne et al. 1996; Goodman et al. 1973). Copper precipitates also contribute to an increase in the corrosion resistance (Irvine and Pickering 1963). HSLA-100 processing entails solutionizing, quenching, and tempering at 620–690°C to obtain a martensitic steel with dispersed Cu precipitates (Czyryca et al. 1990a,c; Nichols 1990; Sawhill 1990). The chemical composition of this alloy is reported in Table 1.

HSLA-100 has been extensively investigated in the past two decades. Studies have been completed to optimize heat treatments (Dhua et al. 2003) and also to investigate relationships between strength and microstructure (Vaynman et al. 2008). The mechanical performance of HSLA-100 has been characterized through studies of its fracture behavior (Das et al. 2006; Densley and Hirth 1998) and its ballistic resistance (Martineau et al. 2004).

The HSLA-100 material characterized in this study was provided by ArcelorMittal, as a 1" thick rolled plate. The material was austenitized at 900°C for 31 min followed by a water quench, then heat treated at 580°C followed by air cooling. All the tested samples were machined directly from the material in the received condition.

1.2 TRIP-120

TRIP-120 was based on a previous prototype (EX425) developed to study transformation toughening under high stresses and strain rates. This alloy was strengthened by γ' Ni_3 (Ti, Al) precipitates and warm working (Stavehaug 1990; Olson 1995). The material was designed by modifying the commercial austenitic stainless steel A286.

Using experiments on EX425 to calibrate design models, Sadhukhan (2008) designed a novel TRIP steel, TRIP-120, with a yield stress of 120 ksi and uniform ductility as the primary performance objective. The steel was tailored to sustain biaxial stretching loadings. Numerous design parameters, such as the grain size and the austenite stability, were optimized to delay the coalescence of microvoids while maintaining a high strength level. For precipitation strengthening, a required γ' mole fraction of 0.083 was set by the titanium and aluminium contents, based on an optimal particle diameter of 14.8 nm demonstrated in the EX425 alloy. TRIP-120 is designed for one hour solution treatment at 950°C, followed by 10 h aging at 750°C. The aging temperature was optimized to control the precipitate size and phase fraction in order to meet the strength goal of 120 ksi. The optimal aging time was confirmed experimentally by hardness measurements.

Grain refining was achieved by a dispersion of submicron TiC particles. The TiC is selected for enhanced interfacial adhesion (Lee et al. 2005) in order to delay microvoid softening for enhanced shear localization resistance. Another goal in the design of TRIP-120 was to avoid intergranular fracture, which had limited the ductility of EX425 under dynamic tensile loading. For that purpose, boron and mobyldenum were added to improve grain boundary cohesion. The chemical composition of TRIP-120 is reported in Table 1.

Transformation toughening mechanisms in TRIP steels have been presented and modeled by Olson and Cohen (1972) and Olson (1995). The model has been enriched by Stringfellow et al. to account for the stress state sensitivity in the transformation (Socrate

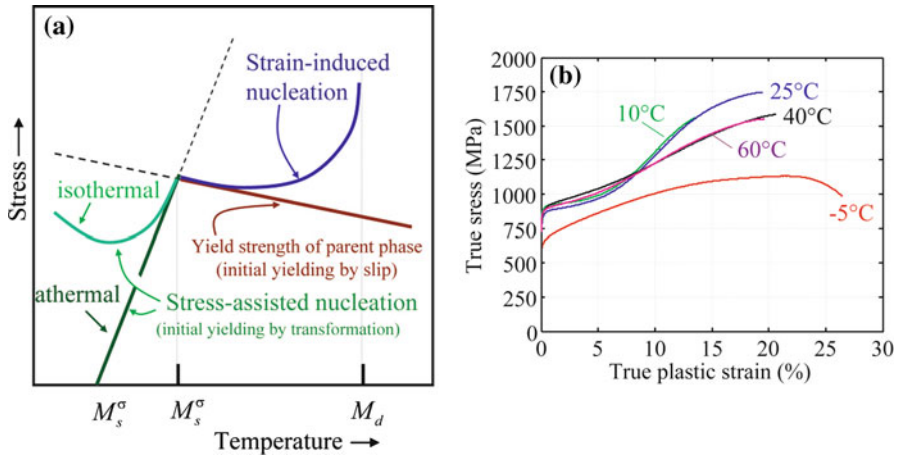

Fig. 1 **a** Schematic representation of strain and stress assisted transformation regimes from ref. Olson (1987), **b** Stress-strain *curves* for isothermal tensile experiments on TRIP-120 at temperatures ranging between −5 and 60°C from ref. Sadhukhan (2008)

1995; Stringfellow et al. 1992). Different transformation regimes operate in austenitic TRIP steels and were presented by Olson (1987) and Haidemenopoulos et al. (1989b). These steels exhibit a characteristic temperature M_s^σ, which marks the transition between stress-assisted and strain-induced nucleation is shown in Fig. 1a. The M_s^σ temperature is dependent on the stress state and is lower in pure shear than in uniaxial tension. Maximum uniform ductility in TRIP steels is usually obtained when M_s^σ is 25 to 30°C below the operating temperature. In this first TRIP-120 prototype, the M_s^σ temperature was measured at 36°C in tension corresponding to a predicted value of 21°C in shear.

Quasi-static isothermal tensile tests ($\dot{\varepsilon} = 1.31 \times 10^{-4}\,\mathrm{s}^{-1}$) on TRIP-120 were performed at different temperatures ranging from −5 to 60°C. The engineering stress-strain curves are reported in Fig. 1b for all the conducted experiments. The shape of the curves depends on the extent of martensitic transformation, which is highly sensitive to temperature. At temperatures $T = 10$°C and $T = 25$°C, where the transformation is stress-assisted, high strength levels are achieved, and a typical sigmoidal shape is observed in the stress-strain curves (Olson and Azrin 1978). At temperatures above the M_s^σ ($T = 40$°C and $T = 60$°C) the transformation is strain-induced and the maximum uniform ductility is achieved.

2 Experimental methodology

2.1 Kolsky bar apparatus

A stored-energy Kolsky bar apparatus previously developed for dynamic friction studies (Espinosa et al. 2000a,b), see also Gilat and Pao (1988), was used in this investigation. It consists of two 25.4 mm diameter 7075-T6 aluminum alloy bars. The incident bar and the transmission bars are 2.3 and 1.9 m long, respectively. To minimize the friction resistance, each bar is supported by a series of recirculating fixed-alignment ball bearings (INA KBZ16PP). The compression/tension and shear loading pulses are generated by the sudden release of elastic energy stored in the incident bar. The energy is produced by hydraulic double acting actuators (Espinosa et al. 2000b).

A Vishay 2,311 signal conditioner and a Tektronix TDS520C digital memory oscilloscope were used to amplify and record the signals on the gage stations located on the incident and transmitted bars. These signals were then processed to compute stress, strain and strain rate evolutions assuming the sample is in equilibrium (Kolsky 1949). To compute the plastic strain, the initial linear part of the stress strain curve was used to determine a tangent initial stiffness combining both elasticity and transient effects. By doing a correction similar to a quasi-static elastic-plastic strain partitioning, the plastic strain-stress curves were obtained as well as the plastic strain-strain rate from the dynamic data. Yield stresses at 0.2% strain were determined from these curves.

2.2 Tension and torsion specimen design

Dynamic tensile tests were conducted on both TRIP-120 and HSLA-100 specimens with cylindrical dog-bone specimens, Fig. 2. The specimens were screwed on both the incident and transmitter bars with 1/4”-28UNS-2A threads. The alignment of the two bars was

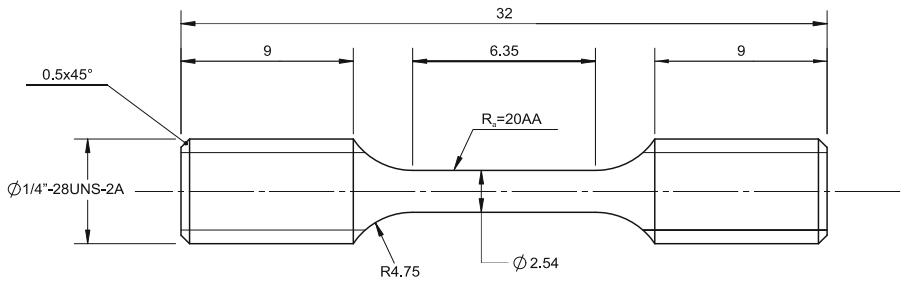

Fig. 2 Dogbone tensile specimen drawing. All the dimensions are in millimeters except the thread

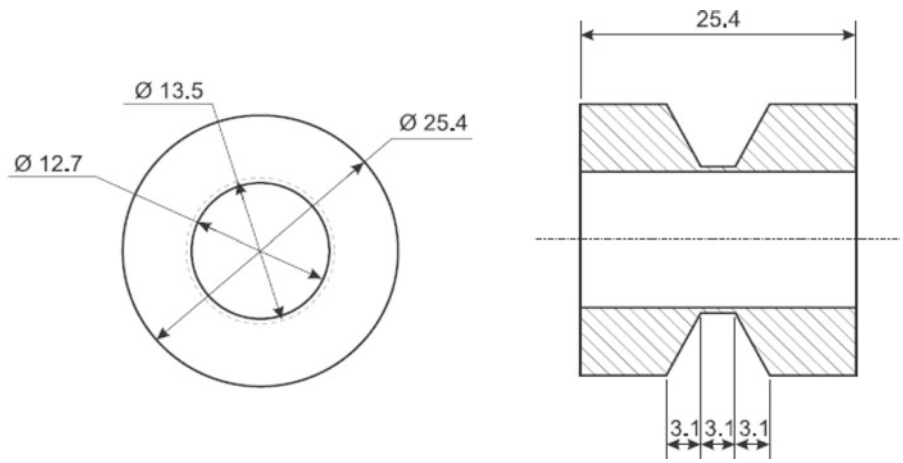

Fig. 3 Thin wall torsion specimen drawing. Dimensions are in mm

adjusted to eliminate bending and shear during the test. In order to achieve high strain rates, the gage length (L_s) was designed as small as possible but not too small compared to the other dimensions of the specimen, such as the transition radius, so that edge effects do not induce a non-uniaxial state of stress (Gray 2000). The geometry used in this investigation was also employed in previous studies (Vaynman et al. 2006). All samples were machined in the longitudinal direction.

Dynamic torsion tests were conducted on thin wall torsion specimens whose geometry is reported in Fig. 3. The gage section of the specimen was machined on a lathe with a conformed tool to properly shape the gage section. The gage section of each sample was then ground with a straight wheel after mounting the specimen on a shaft. This process ensured the coaxiality of the inner and outer cylindrical surfaces of the gage section, giving a uniform thickness in the gage region. The roughness of each gage section (R_a) was approximately 0.8 µm as measured with a stylus profilometer (Mitutoyo Surftest 211). The dimensions of each specimen were measured with a digital caliper (Mitutoyo CD-6"B).

The cylindrical specimens were directly bonded to the extremities of the Kolsky bars with 3M^{TM} Epoxy Adhesive DP460, which has a shear strength of 31 MPa. Before gluing, the surfaces of the sample and the bars were ground with 60/P60 grit sandpaper and cleaned with ethanol and then acetone. In order to minimize the reflection from the bar-specimen interfaces, a thin film of glue was spread over the ends of the bar and then axial pressure applied to squeeze out excessive glue. A cylindrical clamp was used during the glue curing to ensure axial alignment between the sample and the bars.

2.3 High speed photography

Images during the torsion experiments were recorded using high-speed photography. A Cordin 220-8 gate intensified CCD camera was used. This camera can record eight 767 × 574 pixel monochromatic photographs with exposure times adjustable from 10 ns to 1 ms in 10 ns steps and with inter-frame times between 10 ns and 10 ms in 10 ns steps with independent control of each frame. In order to get sufficient magnification,

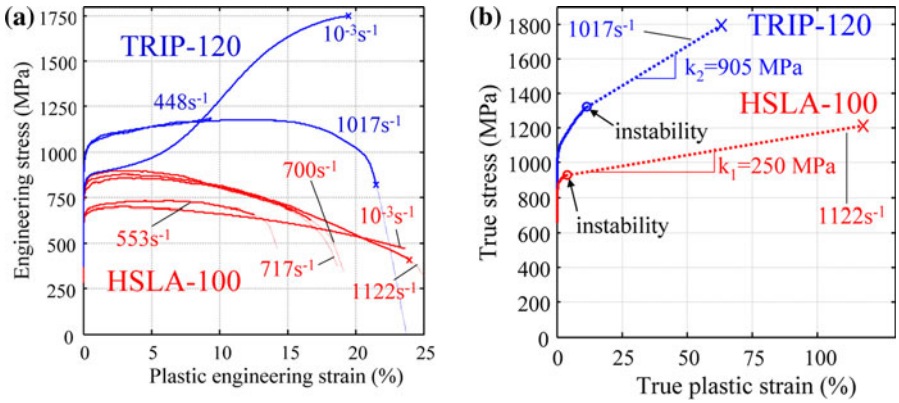

Fig. 4 **a** Engineering stress as a function of the engineering strain for tensile experiments on TRIP-120 and HSLA-100; **b** True stress strain *curves* for dynamic tensile experiments at the highest tested strain rate. The tests were performed under quasi-static and dynamic loading conditions at different strain rates. A *cross* at the end of the *curves* indicates fracture (dynamic fracture was associated to the onset of a strain rate jump)

an internally focused long-distance microscope model K2 by Infinity Photo-optical Company was used. The resolution achieved with this setup was 6.1 µm/pixel, which corresponded to a field of view of 4.7 × 3.5 mm. To achieve sufficiently short exposure times (a few microseconds or less), three 150 W tungsten–halogen LS86/110 lamps by Fiberoptics Specialties, Inc. were used to illuminate the gage section.

The evolution of lines lightly scribed on the gage section of the specimen was used to track the local strain field within the gage section. The average width of the scribed lines was 60 µm. Local strains were finally computed from the optical images using an equal distribution of approximation domains of 150 µm in width over the gage part axis, centered on a selected scribed line present on all the recorded pictures. Denoting the axial coordinate of the sample gage part as x ($0 < x < 3.1$ mm), an average slope $\alpha(x_m)$ was determined on each approximation domain centered on x_m, allowing the computation of the local strain $\gamma(x_m) = \tan\alpha(x_m)$.

3 Results from tension tests

3.1 HSLA-100

HSLA-100 was tested under tension for a range of strain rates from $10^{-3}\,\mathrm{s}^{-1}$ (quasi-static) to $1{,}121\,\mathrm{s}^{-1}$ (achieved with the Kolsky bar apparatus). The engineering stress vs. engineering plastic strain is reported in Fig. 4a for all the conducted experiments. A cross at the end of the curve indicates that fracture occurred within the loading pulse. Fracture was achieved only at the highest tested strain rate, $\dot{\varepsilon} = 1,121\,\mathrm{s}^{-1}$, at an engineering plastic strain ε_p^{en} of 24%. Measured values for each experiment are reported in Table 2. The

Table 2 Tensile tests conducted on HSLA-100

Strain rate (s^{-1})	Yield stress $\sigma_{Y_{0.2}}$ (MPa)	Plastic strain at peak stress (%)	Recorded fracture during initial pulse	True stress at fracture (MPa)	True strain at fracture (%)
10^{-3}	659	2.9	–	–	–
553	670	6.3	No	–	189
700	813	3.1	No	–	169
717	788	2.9	No	–	193
1,122	810	3.1	Yes	1,216	117

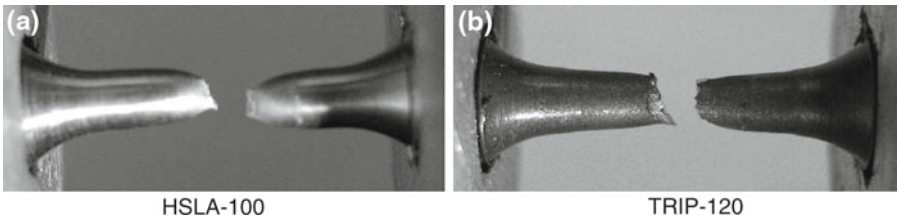

Fig. 5 Post mortem optical images of tensile samples, **a** HSLA-100 tested at $1,122\,\mathrm{s}^{-1}$, **b** TRIP-120 tested at $1,017\,\mathrm{s}^{-1}$

measured stress strain curves highlight moderate strain rate sensitivity in HSLA-100, with an increase in yield stress above $700\,\mathrm{s}^{-1}$. Necking appeared early during the loading ($2.9\% < \varepsilon_p^{en} < 6.3\%$), followed by softening typical of post-peak stress. The post necking ductility was corroborated by post mortem imaging of the sample, which exhibited a smooth necking profile, Fig. 5a, with significant reduction in cross-sectional area after fracture. True strain at fracture was computed as $\ln\left(A_0/A_f\right)$, A_0 being the cross section area of the gage section before the test and A_f the area of the fracture surface measured after the test. The area of the fracture surface was measured using SEM images and led to true strain at failure of 117% (HSLA-100 specimen tested at $1,122\,\mathrm{s}^{-1}$).

3.2 TRIP-120

Two dynamic tension experiments on TRIP-120 were performed at $\dot{\varepsilon} = 448\,\mathrm{s}^{-1}$ and $\dot{\varepsilon} = 1{,}017\,\mathrm{s}^{-1}$. The engineering stress vs. engineering plastic strain curve is reported in Fig. 4a. Fracture was reached during the loading pulse only for the experiment at the highest strain rate. At $\dot{\varepsilon} = 1,017\,\mathrm{s}^{-1}$, the ultimate engineering plastic strain at fracture was 21%, which is close to the value of 19% reached under quasi-static loading at room temperature.

Under quasi-static loading conditions, the stress-assisted martensitic transformation contributes to additional strain hardening and gives the stress-strain curve a sigmoidal shape. The characteristic shape has already been observed and modeled in TRIP steels subjected to stress-assisted transformations (Olson and Azrin 1978). Under dynamic loading the sigmoidal shape is not observed. This is the case because adiabatic heating leads to a rapid increase in temperature (above M_S^σ), which results in a strain-induced martensitic transformation. The material undergoes plastic deformation prior to martensitic transformation. The lower strength at failure observed for dynamic loading versus quasi-static loading is a direct result of less martensitic transformation, which is limited by the adiabatic heating of the material. At strain rates greater than $1{,}000\,\mathrm{s}^{-1}$, necking develops in TRIP-120 at an engineering plastic strain of $\varepsilon_p^{en} = 11.5\%$, which is higher than that observed in HSLA-100 ($\varepsilon_p^{en} = 3.1\%$) under the same conditions.

The two experiments conducted under adiabatic conditions at $448\,\mathrm{s}^{-1}$ and $1,017\,\mathrm{s}^{-1}$ do not show significant variations in yield stress and hardening rate. Under dynamic loading, the yield stress was 18–19% higher than that observed under quasi-static loading. The variations in yield stress observed between quasi-static and dynamic experiments may be attributed to the different yielding modes: the material is yielding by transformation for the quasi-static case ($T < M_S^\sigma$) whereas it is yielding by slip in the dynamic case ($T > M_S^\sigma$), as indicated in Fig. 1a.

3.3 Comparison of HSLA-100 and TRIP-120 performances in tension

Tensile tests results for HSLA-100 and TRIP 120 are summarized in Tables 2 and 3, respectively. In the fourth column of the tables we report those cases in which fracture occurred during the initial stress wave pulse. Note that even when fracture did not occur during the incident pulse, as recorded from the gage signals, the samples fractured due to secondary wave reflections. Post mortem imaging allowed estimation of the fracture strain. Using this information, a comparison based on true stress-strain curves is done in Fig. 4b. At strain rates above $1,000\,\mathrm{s}^{-1}$, we measured true strain at failure of 117% for HSLA-100 and 63% for TRIP-120. This difference in ultimate strain was confirmed by the post mortem optical pictures presented in Fig. 5, in which HSLA-100 showed more pronounced and more diffuse necking than TRIP-120. Although the strain at fracture in TRIP-120 is smaller than HSLA-100, the instability is delayed, which means that TRIP-120 has higher uniform ductility than HSLA-100. Moreover the hardening modulus, k_2, of TRIP-120 is 905 MPa,

Table 3 Tensile tests conducted on TRIP-120

Strain rate (s^{-1})	Yield stress $\sigma_{Y_{0.2}}$ (MPa)	Plastic strain at peak stress (%)	Recorded fracture during initial pulse	True stress at fracture (MPa)	True strain at fracture (%)
10^{-3}	837	No softening	–	2,709	47
448	988	–	No	–	63
1,017	995	11.5	Yes	1,790	63

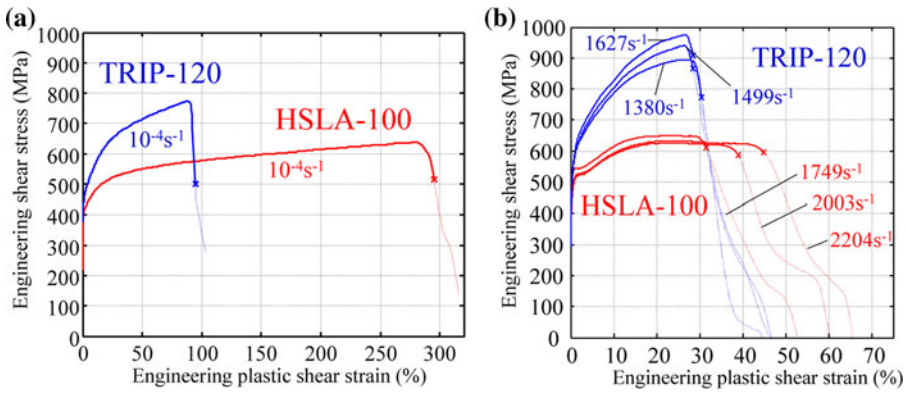

Fig. 6 Engineering shear stress - plastic shear strain *curves* for HSLA-100 and TRIP-120 for **a** quasi-static loadings and **b** dynamic loadings. A *cross* at the end of the *curves* indicates fracture of the sample (dynamic fracture was associated to the onset of a strain rate jump)

which is far bigger than the hardening modulus, $k_1 = 250$ MPa, of HSLA-100.

In terms of strength, the yield stress at 0.2% strain $\sigma_{Y_{0.2}}$ was 995 MPa in TRIP-120 and 810 MPa in HSLA-100 for strain rates on the order of $10^3\ s^{-1}$. The overall energy absorption of TRIP-120 is significantly higher than HSLA-100 as estimated by the average dissipated energy density at fracture $d^f_{tension}$:

$$d^f_{tension} = \int_0^{\varepsilon_f} \sigma^{en} d\varepsilon^{en}_p \quad (1)$$

For a strain rate of $1{,}017\ s^{-1}$, TRIP-120 has a dissipated energy density $d^f_{tension}$ equal to $23.9\ GJ/m^3$, which is 36% higher than that for HSLA-100 with a dissipated energy density of $17.6 GJ/m^3$ at $1{,}122\ s^{-1}$.

It should be noted that the performance reported in this study for TRIP120 has not reached its full potential. It has been recently observed that the current heat treatment used in the tested TRIP120 gives rise to a cellular reaction occurring at the grain boundaries, which is believed to limit the fracture ductility. Evidence of this cellular reaction is presented later in Sect. 5.3.1. Ongoing efforts to eliminate this cellular reaction in TRIP-120 while still achieving the strength goal of 120 ksi are being pursued. With the elimination of this undesired discontinuous precipitate, one would expect to see higher fracture ductility in TRIP 120.

4 Results from torsion tests

4.1 Average behavior

4.1.1 HSLA-100

HSLA-100 was tested in torsion over a range of strain rates, varying from $10^{-4}\ s^{-1}$ (quasi-static) to $2{,}204\ s^{-1}$. The engineering shear stress vs. engineering plastic shear strain is reported in Fig. 6a for the quasi-static experiments and in Fig. 6b for the dynamic experiments. These two figures are plotted with the same stress scale to better identify strength variations between quasi-static and dynamic responses. Specific values for these experiments are reported in Table 4. During all dynamic torsion experiments, failure of the specimen was reached during the first loading pulse, which is represented by a cross in Fig. 6. Sample failure was associated to a sharp increase in strain rate

Table 4 Torsion test results of HSLA-100

Strain rate (s^{-1})	Yield stress $\tau_{Y_{0.2}}$ (MPa)	Peak stress τ_{max}	Eng. plastic strain at peak stress (%)	Recorded fracture during initial pulse	Eng. plastic strain at fracture	Camera pictures (high speed)	Shear banding
10^{-4}	393	637	280	–	280–296	Post mortem	–
1,749	474	650	23.4	Yes	31.5	No	–
2,003	415	626	23.8	Yes	39	Yes	Yes
2,204	420	633	23.5	Yes	45	No	–

Table 5 Torsion test results of TRIP-120

Strain rate (s^{-1})	Yield stress $\tau_{Y_{0.2}}$ (MPa)	Peak stress τ_{max}	Eng. plastic strain at peak stress (%)	Recorded fracture during initial pulse	Eng. plastic strain at fracture	Camera pictures (high speed)	Shear banding
10^{-4}	407	723	89	–	89–93	Post mortem	
1,380	480	893	26.2	Yes	30.5	No	–
1,499	439	940	26.5	Yes	28.5	Yes	No
1,627	447	974	26.7	Yes	28.5	Yes	No

(examples of such sharp increase in strain rate are reported in Figs. 8 and 10). For HSLA-100, dynamic torsional failure occurred at engineering shear plastic strains γ_p^{en} ranging from 31.5 to 45%, while for quasi-static loading failure occurred at a much larger shear strain ($\gamma_p^{en} = 296\%$). The failure strain computed from the gauge data analysis was found consistent with the uniform strain at failure observed on a grating manufactured on the sample gage region (see Sect. 4.2 for details). During quasi-static pure shear, the HSLA-100 stress-strain curve exhibits moderate hardening for strains in the range $40\% < \gamma_p^{en} < 296\%$. Under dynamic conditions, HSLA-100 yields at a slightly higher stress and exhibits features consistent with the development of an instability prior to fracture. Additionally, the strain at peak stress ranges from 23.5 to 23.8% and is insensitive to the strain rate. The engineering strain at fracture, on the other hand, ranges from 31.5 to 45%.

4.1.2 TRIP-120

TRIP-120 was also tested under torsion over a range of strain rates, varying from $10^{-4}\,s^{-1}$ (quasi-static) to $1{,}627\,s^{-1}$. The engineering shear stress τ^{en} as a function of the engineering plastic shear strain γ_p^{en} is reported in Fig. 6a for the quasi-static experiment and in Fig. 6b for the dynamic experiments. Relevant experimental measurements are reported in Table 5.

At quasi-static loading, fracture was reached at a strain of $\gamma_p^{en} \approx 93\%$, obtained from post mortem analysis of a grating manufactured on the gage region of the sample. In the dynamic experiments, fracture was identified for plastic strains in the range $28.5\% < \gamma_p^{en} < 30.5\%$. TRIP-120 shows moderate strain rate dependence under pure shear. There is an increase in the yield stress between quasi-static and dynamic loading, and there is also a noticeable increase of the peak stress as a function of strain rate.

4.1.3 Comparison of HSLA-100 and TRIP-120 average responses in shear

Results of the torsion tests are summarized in Tables 4 and 5 for HSLA-100 and TRIP-120, respectively. Under quasi-static loading, HSLA-100 exhibits 3 times more strain at failure than TRIP-120 but at the expense of reduced strength and strain hardening. This advantage in elongation to failure is much less pronounced under dynamic loading, where both materials show less

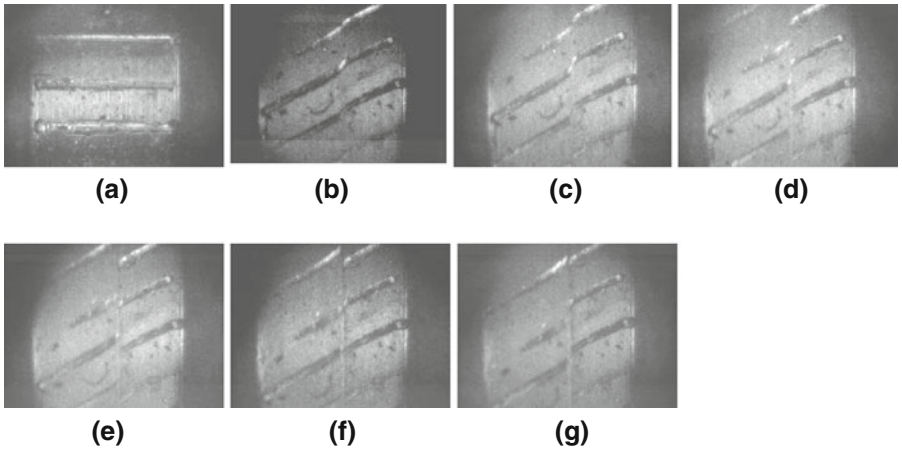

Fig. 7 Photographs of the HSLA-100 specimen surface, in the gage section, tested at $\dot{\gamma} = 2,003\,\mathrm{s}^{-1}$.
a $\gamma^{en} = 0\%$,
b $\gamma^{en} = 32.8\%$,
c $\gamma^{en} = 36.8\%$,
d $\gamma^{en} = 40.8\%$,
e $\gamma^{en} = 44.8\%$,
f $\gamma^{en} = 49.1\%$,
g $\gamma^{en} = 53\%$

ductility. TRIP-120 outperforms HSLA-100 in terms of strength, energy absorption and hardening. The averaged dissipated energy density at fracture, d^f_{shear}, can be computed from Eq. 1 by substituting σ and ε by τ and γ, respectively. At $\dot{\gamma} = 1,627\,\mathrm{s}^{-1}$, the dissipated energy d^f_{shear} is 24.2 GJ/m^3 in TRIP-120, which is an improvement of 25% over the dissipated energy of 19.46 GJ/m^3 computed for HSLA-100 at $\dot{\gamma} = 1,749\,\mathrm{s}^{-1}$.

4.2 Local shear measurements and analysis

4.2.1 HSLA-100

High speed camera measurements were utilized to determine the local shear strain during the dynamic torsion testing of HSLA-100 conducted at an average strain rate $\dot{\gamma} = 2,003\,\mathrm{s}^{-1}$. The photographs, taken with an inter-frame time of 20 µs, are reported in Fig. 7b–g, and the curves are labelled to show the corresponding frames in Fig. 8. A photograph of the initial surface of the sample is shown in Fig. 7a. The first frame under loading, Fig. 7b, shows the development of a shear band as observed from the local slope change in the scribed lines. From this it can be concluded that shear localization started at an engineering shear strain $\gamma^{en} < 32.8\%$. It is worth noting that shear localization in HSLA-100 occurs well before the sudden drop in shear stress in a regime where damage accumulation by void initiation and growth is expected (see Sect. 5). Between frames (d), recorded at $\gamma^{en} = 40.8\%$, and (e), recorded at $\gamma^{en} = 44.8\%$, a transition occurs from smooth lines to much more discontinuous ones. This transition may likely be associated to the sample failure, which is

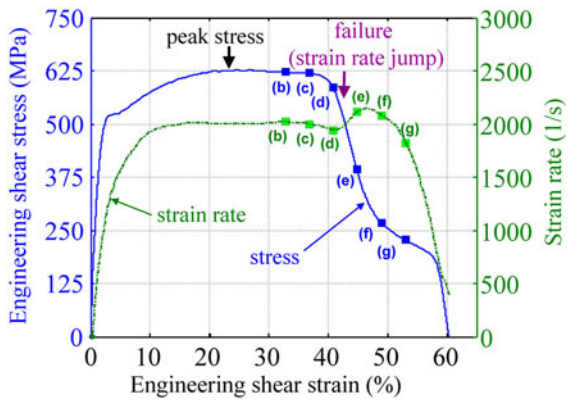

Fig. 8 Engineering shear stress as a function of engineering shear strain for a dynamic torsion experiment conducted on HSLA-100 at $\dot{\gamma} = 2,003\,\mathrm{s}^{-1}$. The *squares* on the *curves* denote the exposure times (*b*) through (*f*) at which high-speed photographs were taken (see Fig. 7)

consistent with the engineering strain at failure of 41.5% assumed from the strain gage signals. In fact, a sharp increase in strain rate was recorded between frames (d) and (e), although no major variation in the magnitude of the strain rate was identified.

4.2.2 TRIP-120

High-speed photography images were also taken throughout the dynamic torsion tests conducted on TRIP-120 at different strain rates (1,499 s^{-1} and 1,627 s^{-1}), in order to monitor the local shear strain. The results from the dynamic torsion test conducted at a strain rate of 1,499 s^{-1} are reported in Fig. 9a–g. The stress, strain and strain states are given in Fig. 10. The photographs were taken with an interframe time of 20 µs.

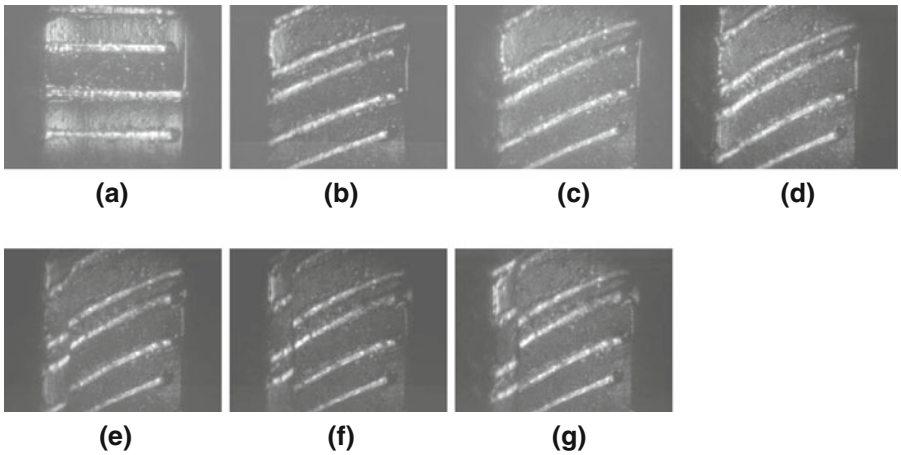

Fig. 9 Photographs of the gage region for TRIP-120 tested at $\dot{\gamma} = 1,499\,\mathrm{s}^{-1}$.
a $\gamma^{en} = 0\%$,
b $\gamma^{en} = 21.8\%$,
c $\gamma^{en} = 25.5\%$,
d $\gamma^{en} = 28.4\%$,
e $\gamma^{en} = 31.2\%$,
f $\gamma^{en} = 35.0\%$,
g $\gamma^{en} = 39.3\%$,

The photographs suggest that fracture occurred between frames (d) and (e), which corresponds to a strain $\gamma^{en} \approx 30\%$. Fracture is manifested by a sharp decrease in stress and a sudden jump in strain rate.

4.2.3 Shear band analysis in HSLA-100 and comparison with HY-100

The experiment conducted on HSLA-100 resulted in shear bands as observed in the photographs reported in Fig. 7. A magnified view of a scribed line is shown in Fig. 11. The whitening within the shear band is used to compute the local slope α^{loc} from which the local strain γ^{loc} in the shear band is computed as $\gamma^{loc} = \tan(\alpha^{loc})$. From this data processing, we identified local strains γ^{loc} within the shear band for three different stages of the deformation, Fig. 12a–c. The magnified views of the shear band show its evolution and ductile stretching, which lead to a local strain γ^{loc} of 764%. This value is consistent with results obtained by Duffy et al. on a higher carbon low alloy martensitic steel (HY-100) having shown local strains up to 600% when tested at $\dot{\gamma} = 1{,}200\,\mathrm{s}^{-1}$ (Duffy and Chi 1992).

The measurement of the local strain γ^{loc} and the shear band width is reported in Table 6 for three different frames captured before fracture, and for the peak stress state where the deformation is assumed to be uniform. The local strain in HSLA-100 was up to 18 times greater than the engineering strain. The results can again be compared with HY-100 for which shear band width varying from 260 µm at $\gamma^{en} = 38\%$ to 30 µm at $\gamma^{en} = 43\%$ were observed (Duffy and Chi 1992). HSLA-100 undergoes less shear band narrowing, showing 27% higher local strains and similar strain rates in the shear band, while being tested at a 52% higher nominal strain rate. The maximum recorded stress was 626 MPa for HSLA-100 and 635 MPa for HY-100. To conclude this comparison, similar behavior in HSLA-100 and HY-100 are observed with a long development of the shear instability from an average strain of ~25% to failure at γ^{en} between 41 and 45%.

4.2.4 Local strain comparison for HSLA-100 and TRIP-120

Local shear strain profiles were computed for both HSLA-100 and TRIP-120, using the method described in Sect. 2.3. In addition, the shear band location x_{loc} was measured directly on the pictures.

As mentioned before, domains with a width of 150 µm were used to compute the local strains. However, as the shear band in HSLA-100 narrowed, the average values were no longer representative of the local strain in the shear band. To overcome this limitation, we substituted the averaged value closest to the shear band position x_{loc} by the value γ^{loc} directly measured on the shear band (Table 6). The results are presented in Fig. 13a for HSLA-100 and Fig. 13b for TRIP-120. For better clarity in the low range of strain in HSLA-100, shear strains higher than 270% were not plotted in this graph. The shear band location x_{loc} was 1.75 mm. On each side of the shear band, at distances $|x - x_{loc}| \geq 0.5$ mm, the strain profile evolution of HSLA-100 show constant values of strain. We also observe a smooth peak centered on x_{loc}.

Four sets of points are plotted in Fig. 13b for TRIP-120 to describe the spatial distribution of strain in the gauge region. Two of them precede the sharp localiza-

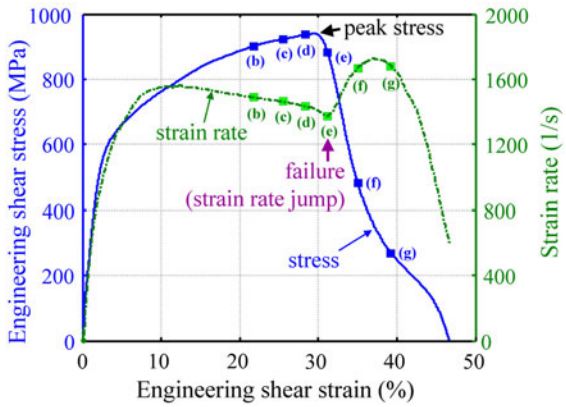

Fig. 10 Engineering shear stress and strain rate as functions of engineering shear strain for a dynamic torsion experiment conducted on TRIP-120 at $\dot{\gamma} = 1,499\,\mathrm{s}^{-1}$. The *squares* on the *curves* denote the times (*b*) to (*f*) at which high-speed photographs were taken (see Fig. 9)

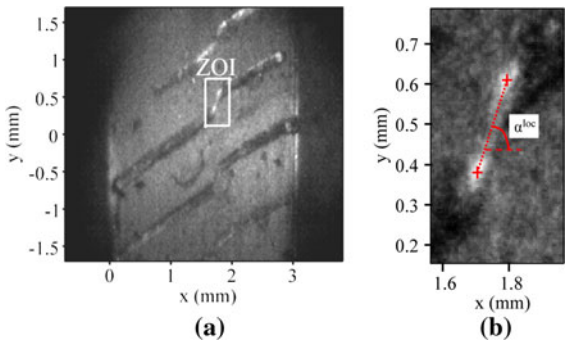

Fig. 11 High-speed camera pictures of shear band in HSLA-100 tested at $\dot{\gamma} = 2,003\,\mathrm{s}^{-1}$, **a** picture captured at $\gamma^{en} = 36.8\%$ showing the monitored surface and the zone of interest (ZOI). **b** A magnified view of the scribed line showing the shear band profile and points used for local strain computation. **a** $\gamma^{en} = 36.8\%$, **b** $\gamma^{en} = 36.8\%$

tion ($\gamma^{en} = 25.5\%$ and $\gamma^{en} = 28.4\%$) and the other two follow the localization onset ($\gamma^{en} = 31.2\%$ and $\gamma^{en} = 35.0\%$). One can notice a strain increase, when considering the two first sets, centered at the location where the material will fracture $x_{loc} = 0.6\,\mathrm{mm}$. The local shear strain increases in the vicinity of this location, while it remains approximately constant otherwise.

In TRIP-120 localization occurred after the maximum shear stress of 940 MPa was reached, while the maximum shear stress in HSLA-100 was 626 MPa. Dynamic fracture in TRIP-120 appears after an average shear strain of $\gamma^{en} = 31.2\%$. This attests to a high

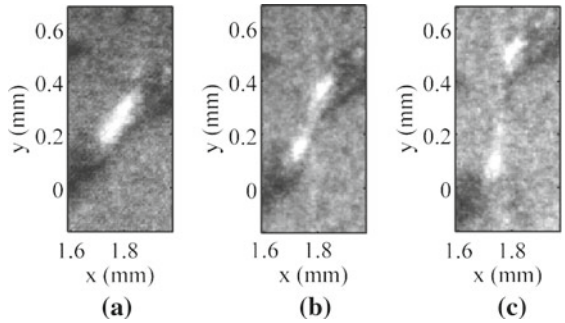

Fig. 12 Magnified views of shear band evolution in HSLA-100 tested at $\dot{\gamma} = 2,003\,\mathrm{s}^{-1}$. **a** $\gamma^{en} = 32.8\%$, **b** $\gamma^{en} = 36.8\%$, **c** $\gamma^{en} = 40.6\%$

shear resistance for TRIP-120 without the benefit of post shear ductility observed in lower strength steels like HSLA-100.

5 Post fracture analysis

5.1 Fracture surfaces of tensile specimens

Fracture surfaces were observed using a FEI NOVA-600 SEM operated at 15 kV. The fracture surface of HSLA-100 is shown in Fig. 14a. Microvoids of width ranging from 0.5 to 2 µm coexist with primary voids larger than 10 µm and smoother surfaces. The analysis of the SEM image leads to the conclusion that HSLA-100 failed in a ductile fashion by void coalescence.

A tensile fracture surface for TRIP-120, shown in Fig. 14b, reveals stretched dimples characteristics of shear fracture together with void coalescence.

5.2 Fracture surfaces of torsion specimens

Fracture surfaces of samples tested under dynamic torsion were also observed using a FEI NOVA-600 SEM. Fracture surfaces for a HSLA-100, tested at $1,749\,\mathrm{s}^{-1}$, and two TRIP-120 samples, tested at 1,380 and $1,627\,\mathrm{s}^{-1}$, are shown in Figs. 15 and 16. All fracture profiles show dimples indicative of ductile shear fracture. As fracture usually propagates dynamically along the cross-section of the specimens, some differences in surface morphology was observed depending on the location within the fracture plane. Therefore, the entire fracture surface was carefully imaged to ensure the consistency of the features reported hereafter. All the fracture surfaces are

Table 6 Local and average strains obtained for HSLA-100 with an interframe of 20 μs and an average strain rate $\dot{\gamma} = 2,003\,s^{-1}$

Frame	γ^{en} (%)	γ^{loc} (%)	γ^{loc}/γ^{en}	$\dot{\gamma}^{loc}$ (s^{-1})	Width of shear band (μm)
Peak stress*	22.6	22.6	1	–	–
b	32.8	103	3.1	$1.6 \cdot 10^4$	139
c	36.8	257	6.9	$7.7 \cdot 10^4$	89
d	40.6	764	18.7	$2.5 \cdot 10^5$	56

* The deformation is assumed uniform

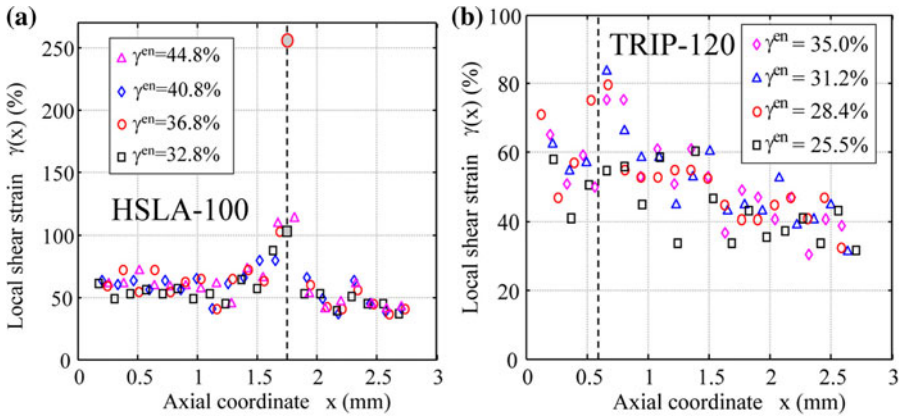

Fig. 13 Local strain measurements obtained **a** for HSLA-100 tested at $\dot{\gamma} = 2{,}003\,s^{-1}$ and **b** for TRIP-120 tested at $\dot{\gamma} = 1{,}499\,s^{-1}$. The fracture locus is indicated by a *vertical black dashed line*. Each strain value is averaged over 150 μm

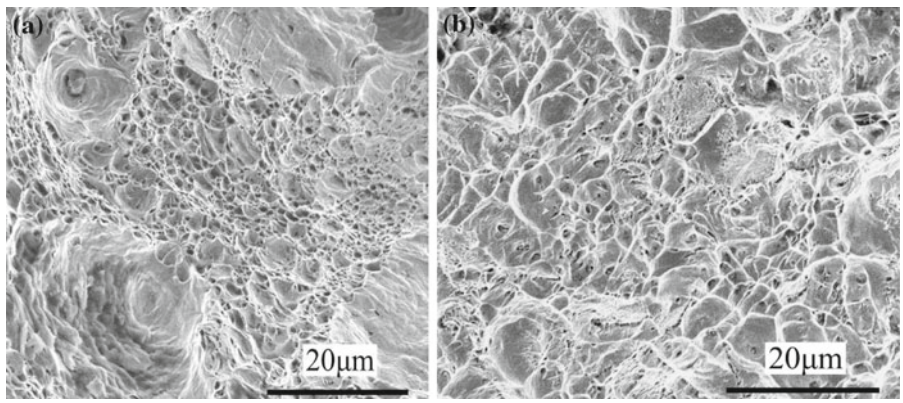

Fig. 14 Tensile facture surfaces for HSLA and TRIP steels: **a** HSLA-100, $\dot{\varepsilon} = 1{,}122\,s^{-1}$, true strain at fracture = 117% **b** TRIP-120, $\dot{\varepsilon} = 1{,}017\,s^{-1}$, true strain at fracture = 63%

reported for a constant orientation of the coordinate system (τ,r), where τ is the circumferential shear direction and r is the radial coordinate.

In Figs. 15 and 16, images shown on the left side are taken at low magnification. Images on the right hand side are taken at high magnification to reveal fracture nucleation sites. The exact location of the magnified images is reported on the left hand side pictures by a square and a letter designation. Slight deviations are observed between the orientation of the local shear and the macroscopic orientation of τ.

In the images of the HSLA-100 fracture surface, Fig. 15, location (A), one can observe stretched dimples typical of ductile shear fracture. Fracture surfaces for TRIP-120 torsion specimens, Fig. 16, reveal different features as a function of strain rate. Dimples at location (C), sample tested at $1,627\,s^{-1}$, exhibit less elongation than those at location (B) that is associated with the sample tested at a lower strain rate of $1,380\,s^{-1}$. Both these samples exhibit dimples with a much reduced elongation when compared to HSLA-100 (Fig. 15, location A).

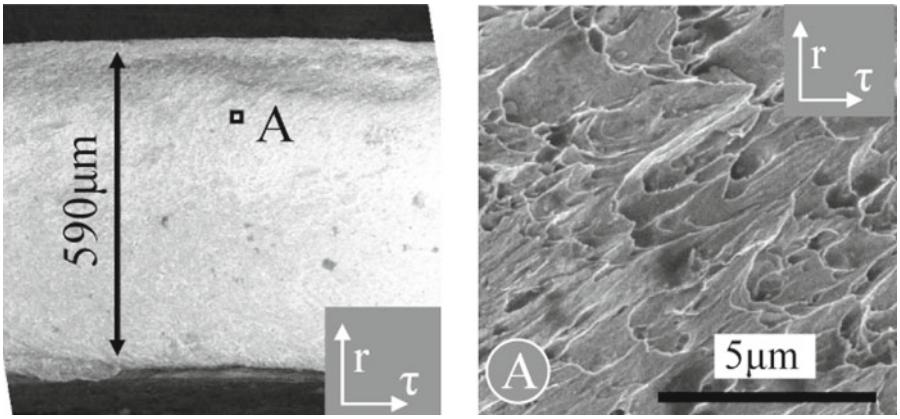

Fig. 15 SEM images of the HSLA-100 fracture surface for a sample deformed at an average strain rate of 1, 749 s^{-1}

5.3 Phase transformation characterization for TRIP-120

5.3.1 Optical microscopy after etching

The dynamic tensile stress strain curves presented in Sect. 3 show lower ultimate strength levels in TRIP-120 for samples tested adiabatically, which could be explained by an inhibition of martensitic transformation under dynamic loading conditions. To test this hypothesis it is desirable to quantify the fraction of transformed martensite after testing. In order to measure the fraction of transformed martensite, fracture surfaces of the shear samples were prepared by metallographically and then observed with an optical microscope. The surface preparation of the samples consisted of grinding, polishing, and etching with a sodium metabisulfate solution (0.5 g Sodium Metabisulfate, 33 cc HCl, 167 H_2O). This particular etchant preferentially etches martensite, which appears dark in the micrographs. The same preparation was performed on a non-tested material (Fig. 17a) and on a portion of the gage region close to the fracture surface of a torsion sample tested at $10^{-3}s^{-1}$ and $1,809s^{-1}$(Fig. 17b, c, respectively). The images shown in Fig. 17 show evidence of fine, strain-induced martensite in the sample tested under adiabatic loading conditions, although no reliable estimate of the fraction of transformed martensite can be assessed from the optical image. The transformation seems to be more pronounced for quasi static loading conditions (Fig. 17b) than for dynamic loading conditions (Fig. 17c). Additionally, Fig. 17a shows evidence of a cellular reaction, appearing as discontinuous precipitates at the grain boundaries darkened by the etchant. Such precipitates are indicated with arrows in Fig. 17a.

5.3.2 Magnetometry measurement in TRIP-120

In order to more precisely quantify the phase fraction of transformed martensite, magnetometry measurements were conducted on torsion samples tested quasi-statically and dynamically at different strain rates. When undeformed, TRIP-120 is fully austenitic, which is paramagnetic, whereas martensite is ferromagnetic. The fraction of transformed martensite was quantified by measuring the saturation magnetization of the sample, which scales linearly with the volume fraction of transformed martensite.

Magnetometry measurements were collected using a Quantum Design Magnetic Property Measurement System with a superconducting quantum interference device (SQUID) detector. A superconducting magnet applied a magnetic field to the sample, and the resulting magnetization of the sample was measured with the SQUID detector. The weight of the samples was restricted (<6 mg) to avoid saturating the SQUID detector. Samples were placed in a gelatin capsule and suspended in the measurement chamber in a nonmagnetic plastic rod. The measurement chamber was held at 300 K throughout the test. The superconducting magnet completed a magnetic field sweep from −5 to 5T, and the corresponding magnetization was recorded for each applied field.

The magnetization saturation was determined by plotting the specific magnetization (M) versus the reciprocal applied field (1/H). The data was extrapolated to infinite field (1/H = 0), and the correspond-

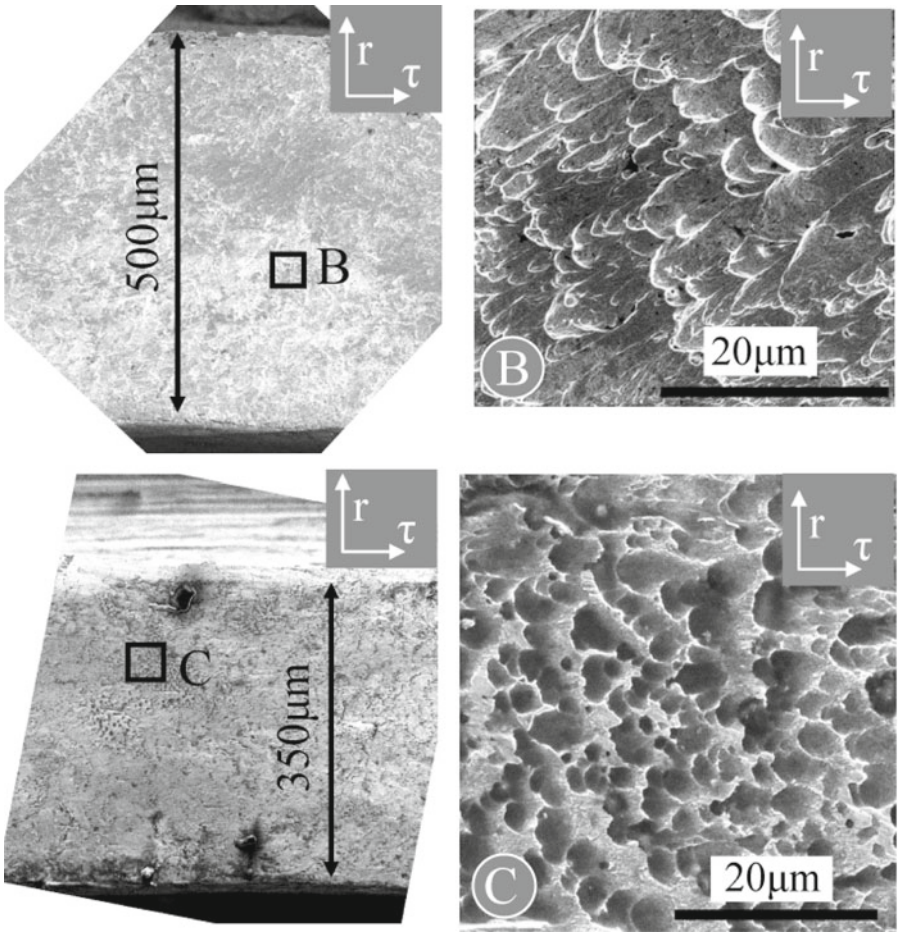

Fig. 16 SEM images of TRIP-120 fracture surfaces. Sample B was tested at an average strain rate of $1,380\,s^{-1}$ and sample C was tested at an average strain rate of $1,627\,s^{-1}$

ing magnetization value was determined to be the magnetization saturation. The measured magnetization saturation was compared to the magnetization saturation of a fully martensitic specimen to determine the fraction of transformed martensite. The magnetization saturation of a fully martensitic (100% transformed martensite) was predicted using the ThermoCalc database. An equilibrium calculation was used to determine the magnetic moment per atom for a fully martensitic sample. Results are gathered in Fig. 18 for an undeformed material, three samples from dynamic tests conducted at average strain rates of 1,809, 1,627 and $1,380s^{-1}$ and a sample from a quasi-static test.

The results show a trend of increasing martensite fraction with higher plastic strain at failure. This is consistent with the expectation that samples able to undergo more transformation will delay necking instability and demonstrate higher uniform ductility. However, the fraction of transformed martensite remains very small after dynamic testing ($3\% \leq f_m \leq 4.5\%$) compared to the level obtained after quasi-static testing ($f_m = 51.6\%$). As we pointed out earlier, at high strain rates, adiabatic heating of the sample leads to an expected reduction of the amount of phase transformation.

6 Summary and conclusions

- Higher dissipated energy in tension and torsion were measured for TRIP-120 in comparison to HSLA-100. TRIP-120 was specifically designed to sustain stable flow at temperatures above room temperature (adiabatic conditions). The marked improvement in uniform ductility was achieved by making use of the transformation-induced plasticity (TRIP) effect to enhance strain hardening. Under uniaxial tension, the plastic strain at necking is 3.7 times greater in the TRIP steel than HSLA-100

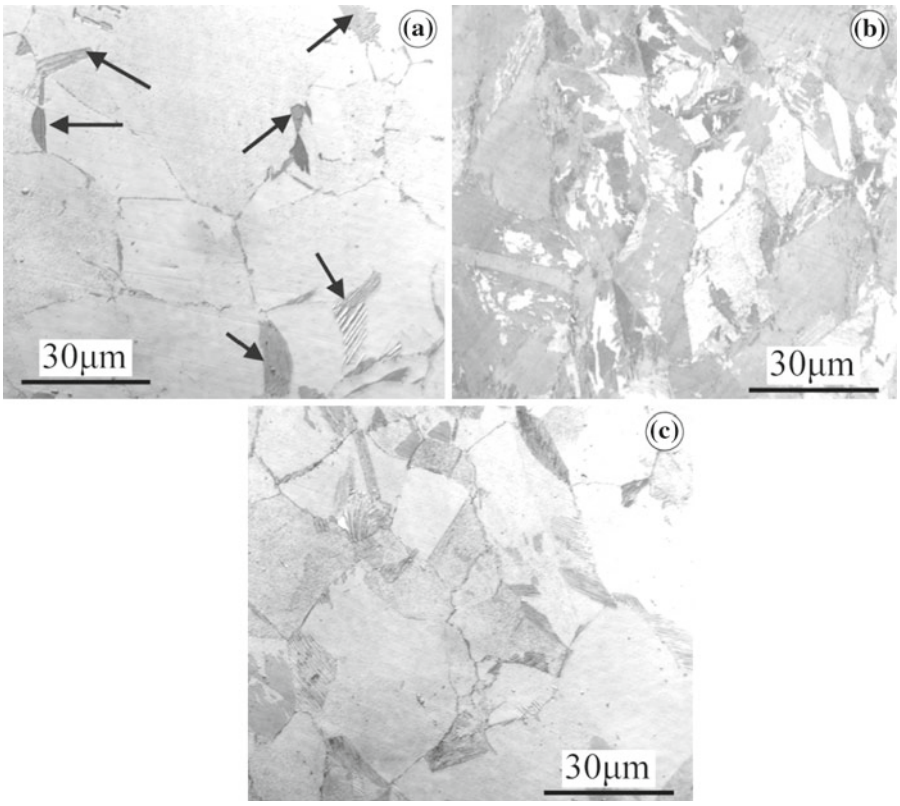

Fig. 17 Optical microscopy images of TRIP-120 etched with 0.5 g Sodium Metabisulfate, 33 cc HCl, 167 H_2O; **a** Initial fully austenitic matrix of undeformed material showing cellular reaction of precipitation strengthening, **b** fine and coarse *darken region* showing evidence of martensite coexist in the sample tested at $10^{-3}\,s^{-1}$, **c** *darker regions* show evidence of fine, strain-induced martensite along the fracture surface for a sample tested at $1{,}809\,s^{-1}$

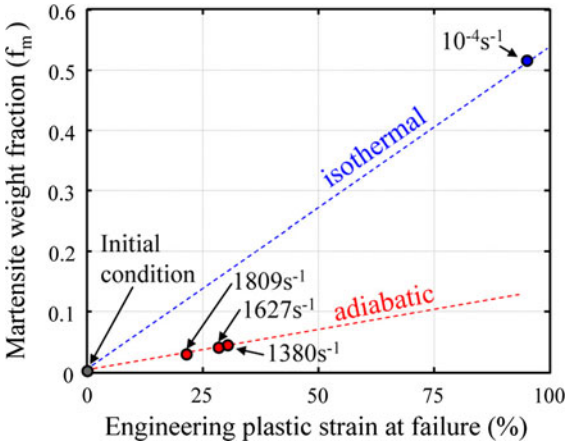

Fig. 18 Martensitic weight fraction f_m as a function of nominal strain at failure for different torsion samples and undeformed material

(Fig. 4). Hence TRIP-120 could be integrated in the design of energy absorption structures of unprecedented performance.

- TRIP-120 shows post-necking ductility in tension, whereas this novel material failed sharply under a pure shear stress state. More diffuse shear banding was observed in HSLA-100, which contributed to larger non-uniform ductility.
- Although TRIP-120 was not optimized for fracture ductility, it demonstrated a large degree of strain hardening in comparison to HSLA-100. Martensitic transformation was quantified in torsion and the strain at failure correlated with the amount of transformed martensite.
- Fracture surfaces showed no evidence of intergranular fracture in TRIP-120. Avoiding intergranular fracture can become particularly difficult in steels of high strength levels. Even after discontinuous decreases in stress during dynamic torsion, SEM images have demonstrated a ductile shear fracture mode.
- The current heat treatment for TRIP-120 leads to the formation of a cellular reaction at the grain boundaries, which likely limits the fracture ductility. Further optimization of the heat treatment to eliminate this cellular reaction should further improve the performance of this alloy under dynamic loading conditions.

Acknowledgements This research was carried out under the financial support by the Office of Naval Research (ONR) under the project entitled "Dynamic characterization of Novel Steel Alloys Resistant to Blast and Fragments" grant number N00014-07-1-1139. The authors would like to acknowledge Alex Wilson and Fred Fletcher at ArcelorMittal for providing HSLA-100 material, and Dr. Sheldon Mostovoy at IIT for conducting quasi static torsion tests. The authors are thankful to Dave Murphy and Susan Palmer at Cordin Inc. for their input on high speed photography.

References

Angel T (1954) Formation of martensite in austenitic stainless steels. J Iron Steel Inst 192:165–174

Batra RC, Kim CH (1991) Effect of thermal conductivity on the initiation,growth and bandwidth of adiabatic shear bands. Int J Eng Sci 29(8):949–960

Bhandarkar D, Zackay VF, Parker ER (1972) Stability and mechanical properties of some metastable austenitic steels. Metall Trans 3:2619–2631

Curtze S, Kuokkala VT, Hokka M, Peura P (2009) Deformation behavior of TRIP and DP steels in tension at different temperatures over a wide range of strain rates. Mater Sci Eng A507:124–131

Czyryca EJ, Link RE, Wong RJ, Aylor DA, Montemarano TW, Gudas JP (1990) Development and certification of HSLA-100 steel for naval ship construction-reply. Nav Eng J 102(4):103–104

Czyryca EJ, Link RE, Wong RJ, Aylor DA, Montemarano TW, Gudas JP (1990) Development and certification of HSLA-100 steel for naval ship construction-reply. Nav Eng J 102(4):104

Czyryca EJ, Link RE, Wong RJ, Aylor DA, Montemarano TW, Gudas JP (1990) Development and certification of HSLA-100 steel for naval ship construction. Nav Eng J 102(3): 63–82

Das SK, Sivaprasad S, Das S, Chatterjee S, Tarafder S (2006) The effect of variation of microstructure on fracture mechanics parameters of HSLA-100 steel. Mater Sci Eng A-Struct Mater Prop Microstruct Process 431(1–2):68–79

Densley JM, Hirth JP (1998) Mixed mode fracture of an HSLA-100 steel. Scr Mater 39(7):881–885

Dhua SK, Mukerjee D, Sarma DS (2003) Effect of cooling rate on the As-quenched microstructure and mechanical properties of HSLA-100 steel plates. Metall Mater Trans A-Phys Metall Mater Sci 34(11):2493–2504

Duffy J, Chi YC (1992) On the measurement of local strain and temperature during the formation of adiabatic shear band. Mater Sci Eng A-Struct Mater Prop Microstruct Process 157(2):195–210

Dunne DP, Ghasemi SS, Yu D (1996) Isothermal transformation products in a Cu-bearing high strength low alloy steel. Isij Int 36(3):324–333

Espinosa HD, Patanella AJ, Fischer M (2000) Dynamic friction measurements at sliding velocities representative of high-speed machining processes. J Tribol Trans ASME 122(4):834–848

Espinosa HD, Patanella AJ, Fischer M (2000) A novel dynamic friction experiment using a modified Kolsky bar apparatus. Exp Mech 40(2):138–153

Gilat A, Pao YH (1988) High-rate decremental-strain-rate test. Exp Mech 28(3):322–325

Goodman SR, Brenner SS, Low JR (1973) FIM-Atom probe study of precipitation of copper from iron-1.4 at pct copper. 1. Field-ion microscopy. Metall Trans 4(10):2363–2369

Gray IGT (2000) ASM handbook. American Society for Metals, Materials Park

Haidemenopoulos GN, Olson GB, Cohen M, Tsuzaki K (1989) Transformation plasticity of retained austenite in stage-I tempered martensitic steels. Scr Metall 23(2):207–212

Haidemenopoulos GN, Grujicic M, Olson GB, Cohen M (1989) Transformation microyielding of retained austenite. Acta Metall 37(6):1677–1682

Hartley KA, Duffy J, Hawley RH (1987) Measurement of the temperature profile during shear band formation in steels deforming at high-strain rates. J Mech Phys Solids 35(3):283–301

Irvine KJ, Pickering FB (1963) Low-carbon steels with ferrite–pearlite structures. J Iron Steel Inst 201:944–960

Kohn G (1976) Effects of TRIP phenomenon on the toughness of Heat Treatable Alloy Steels. Doctoral Thesis, University of California at Berkeley

Kolsky H (1949) An investigation of the mechanical properties of materials at very high rates of loading. Proc Phys Soc 62(11):676–700

Lacroix G, Pardoen T, Jacques PJ (2008) The fracture toughness of TRIP-assisted multiphase steels. Acta Mater 56(15):3900–3913

Lee JH, Shishidou T, Zhao YJ, Freeman AJ, Olson GB (2005) Strong interface adhesion in Fe/TiC. Philosop Mag 85(31):3683–3697

Liao SC, Duffy J (1998) Adiabatic smear bands in a Ti-6Al-4V titanium alloy. J Mech Phys Solids 46(11):2201–2231

Martineau RL, Prime MB, Duffey T (2004) Penetration of HSLA-100 steel with tungsten carbide spheres at striking velocities between 0.8 and 2.5 km/s. Int J Impact Eng 30(5):505–520

Nichols DC (1990) Development and certification of HSLA-100 steel for naval ship construction-comment. Nav Eng J 102(4):102–103

Olson GB, Cohen M (1972) A mechanism for the strain-induced nucleation of martensitic transformations. J Less Common Metals 28(1):107–118

Olson G, Azrin M (1978) Transformation behavior of TRIP steels. Metall Mater Trans A 9(5):713–721

Olson GB, Cohen M (1986) Mechanical properties and phase transformations in engineering materials. In: TMS-AIME, New Orleans, LA, USA

Olson GB (1987) Mechanically induced phase transformation in alloys. Encyclop Mater Sci Eng 4:2929–2931

Olson GB (1995) Transformation plasticity and toughening. In: International seminar on mechanics and mechanisms of solid–solid phase transformations (MECAMAT 95), La Bresse, France, Editions Physique

Patel JR, Cohen M (1953) Criterion for the action of applied stress in the martensitic transformation. Acta Metall 1(5):531–538

Rittel D, Wang ZG (2008) Thermo-mechanical aspects of adiabatic shear failure of AM50 and Ti6Al4V alloys. Mech Mater 40(8):629–635

Sadhukhan P (2008) Computational design and analysis of high strength austenitic TRIP steels for blast protection applications. Doctoral thesis, Department of Material Science, Northwestern University, Evanston

Saha A, Olson GB (2007) Computer-aided design of transformation toughened blast resistant naval hull steels: part I. J Comput-Aided Mater Design 14(2):177–200

Saha A, Jung J, Olson GB (2007) Prototype evaluation of transformation toughened blast resistant naval hull steels: part II. Journal of Computer-Aided Materials Design 14(2):201–233

Sawhill JM (1990) Development and certification of HSLA-100 steel for naval ship construction-comment. Nav Eng J 102(4):103–103

Socrate S (1995) Mechanics of microvoid nucleation and growth in high-strength metastable austenitic steels. Doctoral thesis, Department of Mechanical Engineering, Massachusetts Institute of Technology

Stavehaug F (1990) Transformation toughening of γ'-strengthened metastable austenitic Steels. Doctoral Thesis, Massachusetts Institute of Technology

Stringfellow RG, Parks DM, Olson GB (1992) A constitutive model for transformation plasticity accompanying strain-induced martensitic transformations in metastable austenitic steels. Acta Metall Mater 40(7):1703–1716

Vaynman S, Fine ME, Lee S, Espinosa HD (2006) Effect of strain rate and temperature on mechanical properties and fracture mode of high strength precipitation hardened ferritic steels. Scr Mater 55(4):351–354

Vaynman S, Isheim D, Kolli RP, Bhat SP, Seidman DN (2008) Fine ME high-strength low-carbon ferritic steel containing Cu-Fe-Ni-Al-Mn precipitates. Metall Mater Trans A-Phys Metall Mater Sci 39A(2):363–373

Vernerey F, McVeigh C, Liu W, Moran B, Tewari D, Parks D, Olson G (2006) The 3-D computational modeling of shear-dominated ductile failure in steel. JOM J Miner Metals Mater Soc 58(12):45–51

Zackay VF, Parker ER, Fahr D, Busch R (1967) Enhancement of ductility in high-strength steels. ASM Trans Q 60(2):252–259